

Comparative Analysis of Wavelet-Based Anisotropy Index Calculation for Bathymetric Data

Füsun Er¹, Şengül Ersoy², Yıldray Yalman³

¹ Piri Reis University, Department of Computer Engineering, Tuzla, Istanbul, ror.org/02eq60031

² Piri Reis University, Faculty of Arts and Sciences, Mathematics, Tuzla, Istanbul, ror.org/02eq60031

³ Piri Reis University, Department of Computer Engineering, Tuzla, Istanbul, ror.org/02eq60031

Corresponding author:

Füsun Er, Piri Reis University
fer@pirireis.edu.tr

ABSTRACT

This study investigates the relationship between seabed structures and ship manoeuvrability by applying an anisotropic transformation to bathymetric data. The one of the selected study areas is the downstream section of the Mississippi River in Chalmette, Louisiana, a region characterized by meanders and a maximum depth of approximately 50 meters. The other study areas, which differ in their geomorphological and navigational characteristics, are the Upper New York Bay, Sacramento-San Joaquin River Delta and West Florida Escarpment. Bathymetric data, obtained from NOAA, were converted to fractional anisotropy maps using three wavelet kernels: Coiflet-1, Haar, and Daubechies-4. The anisotropy index was calculated per grid cell to capture directional dependencies in the seabed topography, which may influence ship movements. Statistical analysis, including descriptive statistics and non-parametric tests, was performed to compare the effectiveness of each wavelet kernel. The findings suggest that the Haar kernel is optimal for shallow areas, while the db4 kernel is most effective for detecting anisotropic patterns associated with heading deviations. This study demonstrates the importance of integrating seabed characteristics into predictive models for autonomous navigation, particularly in complex, shallow, and narrow waterways.

Keywords: Inland Waterways, Bathymetric data, Feature extraction, Autonomous navigation, Wavelet analysis

Article History:

Received: 25.03.2025

Revised: 20.07.2025

Accepted: 24.07.2025

Published Online: 26.09.2025

1. Introduction

Maritime navigation and ship maneuverability are influenced by multiple factors, including environmental conditions, vessel dynamics, and operational constraints [1]. One often overlooked yet critical aspect is the impact of seabed topography on ship movement, particularly in confined or shallow waters. Traditional ship route prediction models primarily rely on conventional motion data, including position, speed, and heading. However, integrating seabed characteristics into these models requires robust preprocessing techniques to ensure the data are appropriately structured and analytically meaningful.

Ships navigating through inland waterways, especially in the rugged and mountainous regions far inland, often face a host of challenges [2]. Rapid and turbulent flows can significantly impair ship maneuverability and complicate control. In shallow areas, the ship's hull may interact with the riverbed, causing squat effects that complicate the navigation. When the waterway narrows, the forces of suction and thrust between the ship and the riverbank can limit movement, making it harder to maneuver. Additionally, unpredictable weather conditions, such as sudden waves, can cause the ship to veer off course, further complicating the journey. In the light of such relations, Jörges et al. incorporated seabed topological data to predict ocean wave height [3]. The natural, uneven terrain and steep drops of these river channels only add to the complexity, creating nonuniform water flows that intensify navigational challenges [4] [5].

These complexities highlight the need for more comprehensive models that consider both environmental conditions and seabed characteristics. While traditional ship route prediction models focus primarily on motion data, integrating seabed topography can enhance the accuracy of maneuverability assessments, particularly in challenging environments such as shallow, narrow, or turbulent inland waterways.

Converting seabed topography into a format understandable by machine learning models involves various challenges and considerations. Seabed data are represented by depth measurements in grid-based forms. Effective preprocessing requires feature extraction, where meaningful representations like depth gradients, slope maps, or roughness indices are derived. Directional methods play a crucial role in converting seabed topography data into formats suitable for machine learning models, particularly when the interaction between the vessel's movement and the seabed's structural features is considered. Techniques like directional wavelet transforms and gradient-based feature extraction are commonly used to capture

orientation-specific information [6]. Recent studies have applied 1D wavelet and continuous wavelet analyses to investigate temporal variations in atmospheric parameters such as air temperature, relative humidity, and precipitation, particularly during periods of industrialization and significant climatic events in the Northeastern Black Sea region of Istanbul (Şile) between 1939 and 2012 [7].

In the literature, data-driven route prediction models reveal that most studies focus on the four main AIS features: position, speed over ground (SOG), course over ground (COG), and timestamps [8] [9] [10]. Today, data-driven AI models have become integral in maritime navigation and ship maneuverability studies, particularly when dealing with complex and dynamic environments. These models leverage vast amounts of sensor data, including positional, navigational, and environmental inputs, to make predictions and optimize ship routes in real-time. As the availability of environmental data increases and data-driven approaches continue to advance, these AI models are expected to enhance the safety, efficiency, and accuracy of maritime navigation in the face of ever-changing conditions, particularly in confined or shallow waters. While the use of AIS data is prevalent in the literature [8] [10], very few studies have incorporated environmental data as well [11]. To the best of our knowledge, bathymetric data has not previously been incorporated as a feature in predictive models. This study aims to establish a foundation for feature extraction from bathymetric data.

Changes in seabed depth are among the critical factors that must be considered for accurate route planning, as they influence the direction and speed of ocean currents. This method, which has been successfully applied in the field of medical imaging, is also utilized in various disciplines where directional (anisotropic) properties play a significant role. In geophysics, the power of wavelets for analysis has been exploited for land surface and seabed topography and ocean wave analysis [12] [14] [15] [16] [17]. Wilson *et al.* highlight that the wavelet transform is a local transform, enabling the analysis of bathymetric data at various scales within a given location [13].

The anisotropy analysis combining discrete wavelet transform (DWT) was examined in the spatial variability of SOM and its controlling factors at various scales in a mountainous area [18]. In this study, we applied anisotropic transformation to bathymetric data to examine the relationship between seabed structures and ship maneuvers based on wavelet transformation. Anisotropic filtering emphasizes features based on their directional significance, which is particularly useful when identifying ridges, channels, or slopes that influence vessel maneuverability. This study aims to evaluate the effectiveness of three wavelet kernels—Coiflet, Haar, and Daubechies—in calculating isotropy maps of the sea floor topography of different regions. The goal is to assess their ability to reveal directional dependencies and their potential as tools for detecting heading deviations in maritime navigation. A series of statistical analyses, including a Friedman test and Spearman correlation, were applied to compare fractional anisotropy (FA) values and their relationship with vessel heading deviations (i.e., C-HD). Additionally, a threshold analysis was performed to examine the significance of FA values in distinguishing heading deviations.

In the second section, the data and methodology for the analysis have been explained. The findings are presented in the third section, and the study is concluded in the last section.

2. Datasets and Methodology

This section outlines the general methodology of the study, providing an explanation of the data utilized. The data serve as the foundation for evaluating the relationships between seafloor topography and its indirect influence on the vessel trajectory, enabling an in-depth understanding of the underlying patterns and trends.

2.1. Study Areas

Experiments were conducted on four distinct geographical regions having different environmental and economic properties in terms of maritime transportation. Those are the Lower Mississippi River, Upper New York Bay, Sacramento-San Joaquin River Delta and West Florida Escarpment. Regions of interest are shown as red rectangles on the topographic map, zoomed in to clearly depict the surrounding areas in Figure 1. The Lower Mississippi River stands out for its extensive inland waterway system supporting bulk cargo transport across the central United States [19]. Upper New York Bay differs with its dense urban port infrastructure and high-frequency commercial vessel activity, where Governors Island has caused a navigation obstruction, dividing the maritime routes in the area [20]. The Sacramento-San Joaquin River Delta is distinguished by its shallow, branching channels and environmentally sensitive delta ecosystem [21], where the eastern section of the Benicia-Martinez Railroad Bridge, where inland transportation branches out into Suisun Bay and Grizzly Bay was selected for this study. The West Florida Escarpment is characterized by steep and radical depth transitions, a submarine slope marking the transition between the shallow West Florida Shelf and the deep abyssal plain of the Gulf of Mexico [22]. The following table summarizes the coordinates of the selected regions-of-interest and the grid size with 1-arc resolution (Table 1).

Table 1. Coordinates of Selected Regions of Interest and Grid Size (1-arc Resolution)

ROI#	Name	Coordinates	Resolution	Number of Bathymetric Pixels
R1	Lower Mississippi River	(29° 54' 10" N, 89° 59' 48" W) (29° 56' 52" N, 89° 55' 3" W)	162×285	7059
R2	Upper New York Bay	(40° 39' 36" N, 74° 3' 36" W) (40° 42' 0" N, 74° 0' 0" W)	144×216	20074
R3	Sacramento-San Joaquin River Delta	(38° 2' 12" N, 122° 7' 54" W) (38° 5' 3" N, 122° 2' 34" W)	171×320	34589
R4	West Florida Escarpment	(24° 43' 31" N, 84° 32' 26" W) (24° 50' 24" N, 80° 20' 53" W)	413×693	286166

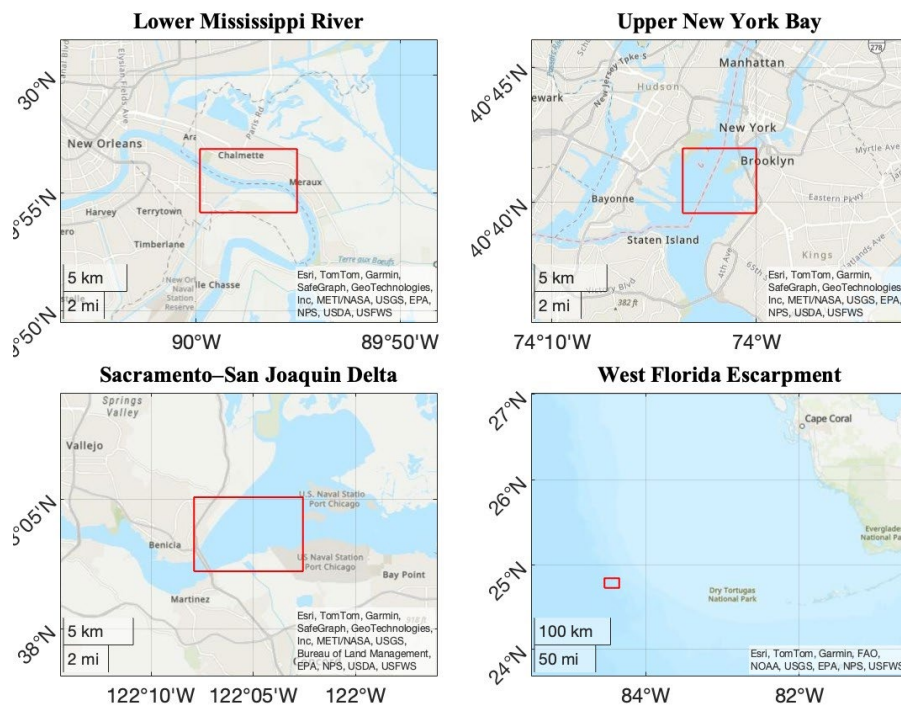


Figure 1. Region-of-interests overlaid on the topographical maps.

2.2. Datasets

In this study, Automatic Identification System (AIS) data and bathymetric grid data were incorporated to investigate the impact of seabed topography on vessel navigation, using the proposed method. The bathymetric grid data were obtained from the National Oceanic and Atmospheric Administration (NOAA), National Centers for Environmental Information (NCEI) Bathymetry, which is freely available on NOAA Bathymetric Data Viewer [23]. The bathymetric data represent the seafloor as a grid of cells, each representing the depth (vertical distance) from the mean sea surface to the seafloor in meters. The data were retrieved from the National Ocean Service (NOS) Bathymetric Attributed Grid (BAG) Mosaic dataset via the NOAA Bathymetric Data Viewer at a one-arc-second resolution (approximately 30 meters at the equator) and were downloaded in Geographic Tagged Image File Format (GeoTIFF) format [24].

In addition to the bathymetric data, a historical raw Automatic Identification System (AIS) time-stamped dataset was obtained from the international data provider Marine Cadastre [25], covering the region-of-interests of this study. The dataset is formed as a CSV (Comma-Separated Values) file per day, where each record is a comma-separated list of attributes that refers to the information transmitted by vessels. It includes various attributes such as positional data (Latitude and Longitude), movement data (Course Over Ground, Speed Over Ground, Heading), and identification or status data (MMSI, timestamp, vessel type, and navigational status). Latitude and Longitude together provide the precise geographical location of the vessel in degrees, with latitude indicating the north-south position relative to the equator and longitude indicating the east-west position relative to the Prime Meridian. Course Over Ground (COG) refers to the actual direction in which the vessel is moving over the Earth's surface, measured in degrees clockwise from true north. This value may differ from the vessel's heading due to environmental factors such as wind or currents. Speed Over Ground represents the vessel's real-time speed relative to

the ground, expressed in knots, and reflects the influence of external forces on the vessel's movement. Heading describes the direction in which the bow of the vessel is pointing, which may not always align with the COG [26] [27]. The ship identification attribute refers to a unique identifier assigned to each vessel, such as the Maritime Mobile Service Identity (MMSI), which enables vessel tracking and identification. The timestamp indicates the exact date and time when the data was recorded, which is essential for constructing and analyzing the trajectory of the vessel over time. Finally, AIS data includes navigational status information, such as 'Underway using engine', which indicates that the vessel is moving through the water under its own propulsion, as opposed to being anchored, moored, or adrift [27].

The obtained raw AIS data contains some missing values, redundant entries, and records that are not related to the scope of this study. To ensure the reliability and accuracy of our analysis, a series of filtering criteria were applied. Firstly, only records within the defined region of interest, specified by latitude and longitude boundaries, were retained. COG, SOG, and Heading are dynamic parameters in AIS data that describe a vessel's movement and orientation. However, these values are only meaningful when the navigational status of the vessel is reported as 'Underway using engine', indicating that the vessel is actively moving under its own propulsion [28]. Therefore, only vessels with this status were included. Furthermore, to focus on relevant maritime traffic, only vessels classified as cargo or tanker types were considered. Records with missing or invalid speed overground (SOG) and course overground (COG) values were excluded to maintain data quality.

2.3. Methodology

A general overview of the methodology applied in this study is presented in Figure 2, grouped into three phases: (1) Data Collection, (2) Data Processing, and (3) Data Analysis, to describe and infer the data.

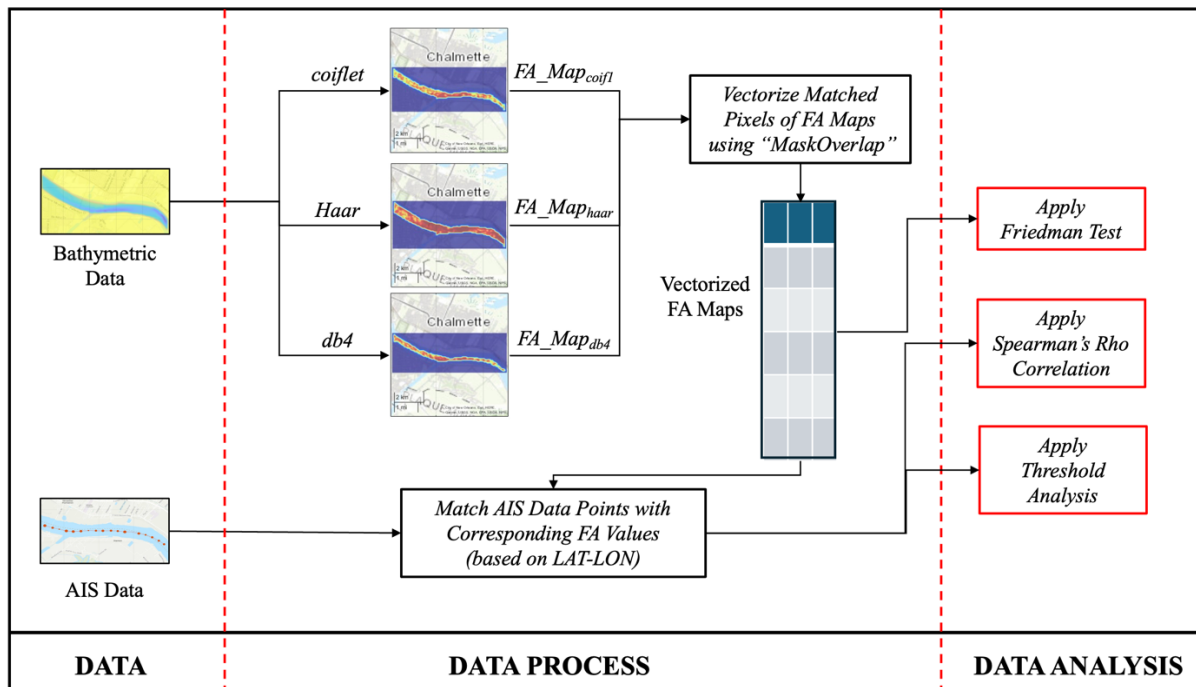


Figure 2. General view to the methodology of the presented study

As mentioned earlier, two different types of data were selected from the matched geographical region: Bathymetric Data in a 1-arcsecond by 1-arcsecond grid and AIS Data labelled with longitude and latitude in degrees. Initially, a procedure was applied to obtain fractional anisotropy (FA) maps based on different wavelet kernels using Algorithm 1, as outlined in the pseudocode (see Section 2.2.1). Since each wavelet kernel could not generate values at every point of the seabed, a mask was created to show the intersection grids, called *MaskOverlap*. The three different FA values generated for each grid cell within the *MaskOverlap* were matched and converted into an array, where the grid cells are in the rows and their corresponding FA values in the columns (Vectorized FA Maps). Then, each AIS data point that fall within *MaskOverlap* was associated with the grid cell of a 1-arcsecond by 1-arcsecond grid, depending on which cell fell within the LAT/LON boundaries. Finally, in addition to descriptive statistics and data characterization methods such as histograms and geospatial visualization, three different inferential methods were applied to the derived data: the Friedman test to assess whether there is a significant difference between the obtained FA maps, Spearman's rho correlation to determine the relationship between AIS data and FA maps, and threshold analysis to identify whether there is a threshold that divides the FA maps into two meaningful regions in terms of vessel heading deviations, indirectly influenced by sea floor topography.

In this research study, a mask (*MaskSeaFloor*) was initially created to exclude non-seafloor areas from the analysis using the obtained bathymetric data, where values equal to or greater than zero represent land, while negative values indicate the underwater region. After calculating isotropy maps, a mask (*MaskOverlap*) is generated for further analysis.

2.3.1 Deriving Anisotropy Maps of Bathymetric Data

The following procedure was applied to convert the bathymetric data into a fractional anisotropy map (Algorithm 1). The aim of this procedure is to calculate an anisotropy index per grid cell that is a decimal number in the range of zero and one. The procedure takes the bathymetric data to be used (bMap) and the name of the wavelet to be applied (wFilter). The bathymetric data, bMap, is a two-dimensional double array with dimensions n (rows) and m (columns), where n and m represent the number of grid cells in the rows and columns, respectively. The parameter wFilter is the name of the wavelet kernel that will be used to calculate horizontal and vertical variations per grid cell, where three different well-known wavelet kernels were applied: Coiflet-1 (coif1), Haar (haar) and Daubechies-4 (db4). Table 2 presents a comparative overview of the mathematical properties of the selected wavelet families. These wavelets differ notably in terms of support width, vanishing moments, and regularity, which influence their ability to capture signal characteristics such as abrupt changes or smooth variations. The support width affects the locality and regularity of the wavelet transform: Haar has the smallest support and is best suited for detecting sharp transitions [29], whereas Coiflet and db4 offer greater smoothness due to wider support. Rather than normalizing this parameter across wavelets, we retained their original configurations to preserve their intrinsic characteristics and evaluate their practical effects in the analysis.

Table 2. Comparative properties of selected wavelet families

Property	Haar	Coiflet	Daubechies
Support Width	1	6	8
Vanishing Moments	1	2	4
Orthogonality	Yes	Yes	Yes
Compact Support	Yes	Yes	Yes
Regularity	Discontinuous	Higher than Haar	Moderate

The Haar wavelet is a simple, piecewise constant function with two coefficients, making it computationally efficient. Despite its lack of smoothness, it is commonly used in introductory studies due to its simplicity. Daubechies is a famous family of wavelets known for its compact support and orthogonality, making it efficient for analysis and decomposition. Coiflet wavelets, similar to Daubechies, have a different shape and are particularly useful for analyzing signals with finite support, with Coif1 being a prominent member of this family, known for its symmetry, compact support, and orthogonality, making it ideal for signal processing applications [15] [29].

The wavelet transform (WT) is an advanced mathematical method that provides scale and location information for spatial variation [18]. The idea is based on a family of wavelets, called mother wavelets, defined by,

$$\varphi_{a,b}(t) = \frac{1}{\sqrt{|a|}} \varphi\left(\frac{t-b}{a}\right), a, b \in \mathbb{R}, a \neq 0$$

Where ‘a’ is called a scaling parameter and ‘b’ is called a translation parameters [30]. The Haar wavelet is the simplest of all orthogonal wavelets and is given as

$$\varphi(t) = \begin{cases} 1 & 0 \leq t < \frac{1}{2} \\ -1 & \frac{1}{2} \leq t < 1 \\ 0 & \text{otherwise} \end{cases}$$

The Daubechies wavelets are one of the orthonormal wavelet families with compact support, on the other hand, Coiflets are similar to Daubechies wavelet differs in the number of vanishing moments [29]. The compact support of Haar coefficients makes them well-suited for capturing sharp variations in the signal [31]. The first line of the pseudocode computes the single-level 2-D discrete wavelet transform (DWT) of the input data bMap using the wFilter wavelet with the ‘dwt2’ function of the MATLAB Wavelet Toolbox (version R2024b; academic use license), producing the horizontal (cH) and vertical (cV) detail coefficients matrices, which are then resampled to match the size of the bMap matrix. In the second line of the pseudocode, a second-order tensor matrix (tensor) is calculated, resulting in a three-dimensional array where $tensor_{i,j,*}$ represents the second-order tensor matrix of the grid cell located at the *i*-th row and *j*-th column. Then the fifth and sixth lines of the pseudocode repeated each grid cells, where an eigen decomposition method was applied to decompose the second-order tensor matrix into its eigenvalues (λ_1, λ_2) and its eigenvectors. The ‘eig’ function of the MATLAB Linear Algebra Toolbox (version R2024b; academic use license) was used in this study to obtain eigenvalues. Finally, as depicted in the sixth line of the pseudocode, an anisotropy value is assigned to currently processed grid cell. If the calculated value is closer to zero, this

means that the geographical area in a 1-arcsecond by 1-arcsecond grid is isotropic. Conversely, if the index is closer to one, it indicates an anisotropic area [32] [33].

Algorithm 1. Procedure for deriving FA Maps from Bathymetric Data

1	$[cH \quad cV] = \text{wavelet_transform}(\text{bMap}, \text{wFilter});$
2	$\text{tensor} = \begin{bmatrix} cV^2 & cV * cH \\ cV * cH & cH^2 \end{bmatrix}$
3	for $i=1:n$
4	for $j=1:m$
5	$[\lambda_1 \quad \lambda_2] = \text{eigen}(\text{tensor}_{i,j,*})$
6	$FA_Map_{wFilter}[i,j] = \left(\frac{ \lambda_1 - \lambda_2 }{\sqrt{(\lambda_1^2 + \lambda_2^2)}} \right)$

The procedure defined in Algorithm 1 was executed three times using different kernels to obtain anisotropy maps, called FA_Map_{coif1} , FA_Map_{haar} and FA_Map_{db4} . Therefore, a second mask ($MaskOverlap$) was obtained from the areas where the anisotropy maps generated by the three kernels overlap which is needed for statistical analysis to apply either paired or unpaired tests, where $MaskOverlap$ is a subset of $MaskSeaFloor$. To minimize data exclusion while maintaining analytical rigor, we generated a secondary mask ($MaskOverlap$) from the spatial intersection of anisotropy maps derived using the three kernels. This approach allowed us to retain only the consistently represented pixels across all kernel outputs, ensuring suitability for both paired and unpaired statistical comparisons. $MaskOverlap$, as a subset of $MaskSeaFloor$, excludes only a minimal portion of the original dataset. We deliberately avoided imputing missing values (e.g., by zero-padding), as such practices may introduce artificial variance and compromise the reliability of statistical inference.

2.3.2 Matching AIS Data with FA Maps

Each AIS data point that fell in $MaskOverlap$ was associated with the grid cell of a 1-arcsecond by 1-arcsecond grid, depending on which cell fell within the LAT/LON boundaries. Then, the COG-Heading Deviations (C-HD) of the vessels were calculated by getting the absolute value of the difference between the COG and Heading of vessels, to analyse the relationship between bathymetry and radical deviations from the route, where COG refers to the actual direction of motion and Heading is the direction in which a vehicle or a vessel is pointing at any given moment.

2.3.3 Analysis

The following statistical tests were applied on FA_Map_{coif1} , FA_Map_{haar} and FA_Map_{db4} : Descriptive statistics were calculated for the pixels masked by $MaskSeaFloor$, and a histogram was plotted. For the areas within $MaskSeaFloor$, a paired non-parametric statistical significance test was applied to assess whether there was a significant difference between the calculated FA Maps. The 'friedman' function of MATLAB Statistics and Machine Learning Toolbox (version R2024b; academic use license) was utilized for this purpose, which is a non-parametric alternative to the repeated measures ANOVA.

The correlations between the matched SOG value and each of the three FA values, and between the matched C-HD values and each of the three FA values were calculated using Spearman's rank correlation method, resulting in six Spearman's rho values that indicate if there is a meaningful monotonic relationship between these variables. The 'corr' function with the type of parameter of 'Spearman' of the MATLAB Statistics and Machine Learning Toolbox (version R2024b; academic use license) was used to calculate Spearman's rho values.

A threshold analysis was conducted to determine if there exists a statistically meaningful threshold to divide FA values into two groups, such that the corresponding C-HD values yield significantly different outcomes in each group. To perform this analysis, a set of thresholds ranging from 0.1 to 0.9, with intervals of 0.05, was used to partition the FA values into 'high' and 'low' groups. For each threshold value, a two-sample t-test was conducted to compare the C-HD values corresponding to the high and low FA groups. The p-values obtained from the t-tests were stored for each threshold and each type of FA value. A threshold vs p-value graph was also plotted to visualize the relationship between different threshold values and their corresponding p-values. This graph helps in identifying the threshold at which the p-value indicates a statistically significant difference in the C-HD values.

3. Experimental Results and Discussion

This section presents the collected data, investigates the analysis of the isotropy of the bathymetric data, and finally the correlation between vessel behavior and the isotropy of the seabed in selected regions of interest.

3.1. Bathymetric and AIS Data

Figure 3 presents the bathymetry maps of the regions of interest (ROI). The first selected region is the lower bank of the Lower Mississippi River, characterized by its meanders, with a maximum depth of approximately 50 meters (Fig. 3). Upper

New York Bay is shallower than the Lower Mississippi River, with the shallowest area of Upper New York Bay approximately half as deep as the shallowest area of the Lower Mississippi River. Among all four regions of interest, the shallowest is the Sacramento–San Joaquin Delta and the deepest is the West Florida Shelf, with maximum depths of approximately 30 meters and 3500 meters, respectively. The West Florida ROI contains abrupt bathymetric transitions.

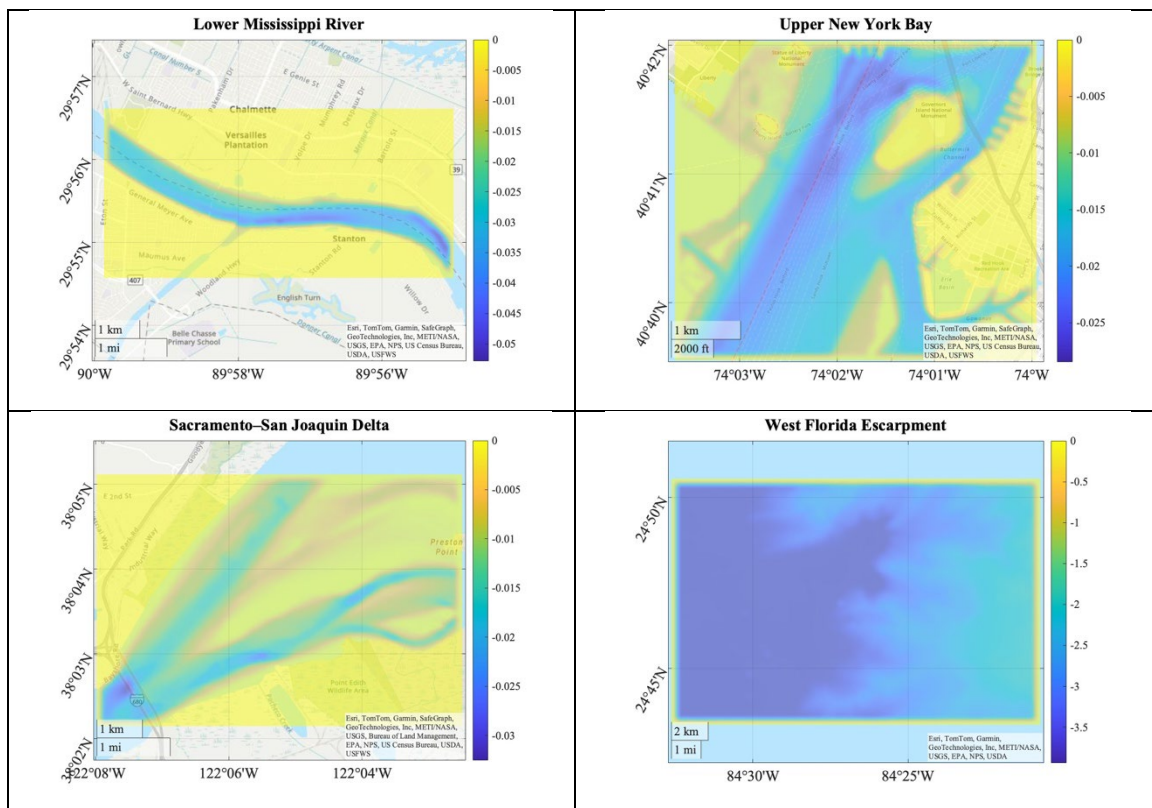


Figure 3. Bathymetric data at one arc-second resolution for all regions of interest overlaid on a street map

AIS data points were collected across all four regions of interest between January 1 and January 31, 2023. Figure 4 shows one of the collected trajectories, consisting of 17 AIS data points overlaid on the topographical map of the Lower Mississippi River region-of-interest, where the size of the red circles represents the C-HD values, with larger circles indicating higher heading deviations of the vessel.



Figure 4. Trajectory with Heading Deviations, Marker Size Represents Deviation Magnitude

Table 3 presents the descriptive statistics of SOG, COG and C-HD for the collected AIS data points, exhibiting high variance as these parameters have a broad range of values. The number of AIS data points varies depending on traffic density. The highest number of AIS points was collected from the Upper Bay, a densely trafficked port area. In contrast, fewer AIS data points were obtained from the West Florida Escarpment region, an open sea area where vessel density is more dispersed. For each region, statistical measures (minimum, maximum, mean, and standard deviation) are provided for four key AIS features: Speed Over Ground (SOG), Course Over Ground (COG), Heading, and Course–Heading Difference (C-HD). These metrics help illustrate the variability and navigational behaviors within each region. In ROI#2 (Upper New York Bay), the Course–

Heading Difference (C-HD) exhibits the highest variability among all regions, as indicated by its standard deviation of 78.9. This large variation may be attributed to several factors specific to dense port environments. The influence of strong tidal currents and wind patterns in this harbor area can cause vessels to drift, increasing the difference between the direction a vessel is pointing (heading) and the direction it is actually moving (COG). In ROI#3 (Sacramento Delta), the Course-Heading Difference (C-HD) shows the lowest standard deviation (1.8), indicating minimal discrepancy between vessel heading and actual course over ground. This low variability can be attributed to the geographical and operational characteristics of the region. The Sacramento Delta consists mainly of narrow, shallow inland waterways, where vessels are required to follow well-defined and constrained routes with limited room for maneuvering.

Table 3. Descriptive statistics for AIS data points collected within the region of interest

ROI#	AIS Data Points	AIS features	min-max	mean	std
R1	19608	SOG	5.2-13.9	10	1.8
		COG	86.7-320	210.4	91.6
		Heading	88-315	210.09	90.7
		C-HD	0-13.6	2.9	2.6
R2	173978	SOG	0-30.3	10.7	7.3
		COG	0-359.9	143.4	104
		Heading	0-359	151.3	110.1
		C-HD	0-359.9	44.2	78.9
R3	3526	SOG	7.9-13.3	11	1.6
		COG	52.5-272.1	166.5	90.1
		Heading	49-271	165.9	91.8
		C-HD	0.2-7.3	2.6	1.8
R4	1032	SOG	14.5-14.6	14.6	0.001
		COG	15.2-18.5	17.5	1.2
		Heading	12-15	14.2	1.3
		C-HD	2.8-3.7	3.2	0.3

3.2. Anisotropy Analysis

Table 4 presents the descriptive statistics of the isotropy indices computed from the seafloor using three different wavelet filters (coif1, Haar, and db4) across four regions of interest (ROIs: R1–R4). The distributions of these indices are visualized as histograms for R1 in Fig. 5, with the spatial extent masked by the *MaskOverlapFloor*.

Table 4. Statistics of the Isotropy Indices of the Sea Floor

ROI#	Kernels	Geometric Mean	Geometric Std	Arithmetic Mean	Median	Kurtosis	Skewness
R1	coif1	0.810	1.398	0.845	0.923	5.459	-1.701
	haar	0.925	1.216	0.938	0.985	16.661	-3.444
	db4	0.820	1.391	0.853	0.933	5.704	-1.755
R2	coif1	0.752	1.448	0.791	0.856	4.297	-1.333
	haar	0.894	1.267	0.912	0.970	11.616	-2.775
	db4	0.738	1.479	0.781	0.849	3.879	-1.216
R3	coif1	0.845	1.343	0.872	0.942	7.294	-2.060
	haar	0.938	1.198	0.949	0.993	19.717	-3.788
	db4	0.779	1.437	0.818	0.894	4.496	-1.429
R4	coif1	0.719	1.485	0.762	0.827	3.707	-1.156
	haar	0.849	1.351	0.877	0.956	7.277	-2.104
	db4	0.726	1.480	0.769	0.834	3.752	-1.175

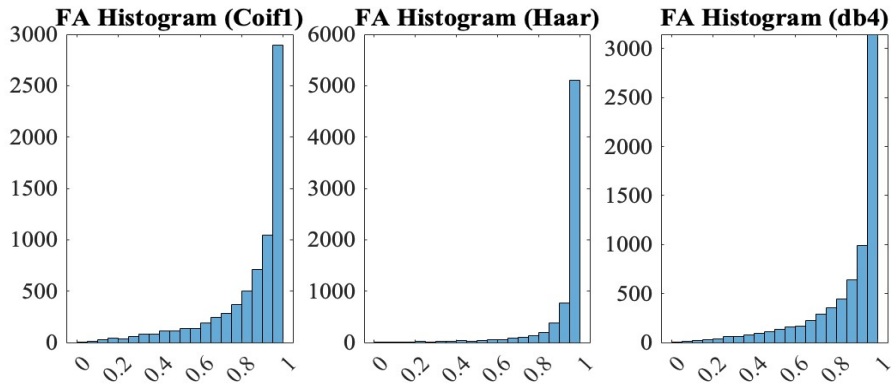


Figure 5. Histograms showing the distribution of FA values derived by Coif1, Haar and db4 wavelet kernels (left-to-right) of the Lower Mississippi River

For each ROI and kernel, the geometric mean, geometric standard deviation, arithmetic mean, median, kurtosis, and skewness are reported. The db4 and coif1 filters often show higher kurtosis, suggesting more peaked distributions. Negative skewness in all cases implies left-skewed distributions, with Haar being the most negatively skewed, especially in R3. Across all ROIs, the arithmetic and geometric mean of the isotropy indices is consistently highest when computed using the Haar wavelet filter, which may suggest its tendency to emphasize higher local isotropy values compared to coif1 and db4. For all wavelet filters and ROIs, the arithmetic means are consistently lower than the corresponding medians, indicating negatively skewed distributions where the majority of isotropy index values cluster at higher levels, with a few lower values pulling down the mean.

The Eigenvalues (λ_1 and λ_2) and FA values calculated for R1: “Lower Mississippi River” were overlaid on the map of the region of interest, calculated using the Coiflet, Haar and db4 wavelet kernels, as shown in Fig. 6, Fig. 7 and Fig. 8, respectively. On the far left, eigenvalue-1 is shown vertically, representing the north-south directional dependency. In the center, eigenvalue-2 is displayed horizontally, indicating the east-west directional dependency. On the far right, the heat map of the calculated FA values is presented. It can be seen that the Haar wavelet kernel is more successful in revealing details in shallow areas, where shallow areas are characterized by abrupt changes in topography. When revealing the north-south direction, db4 is the least effective of the two others.

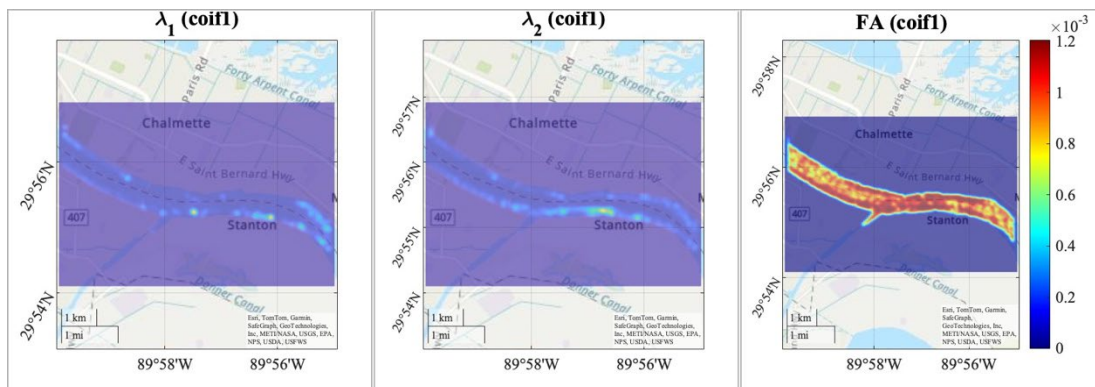


Figure 6. Eigenvalues and FA values calculated using Coiflet wavelet kernel

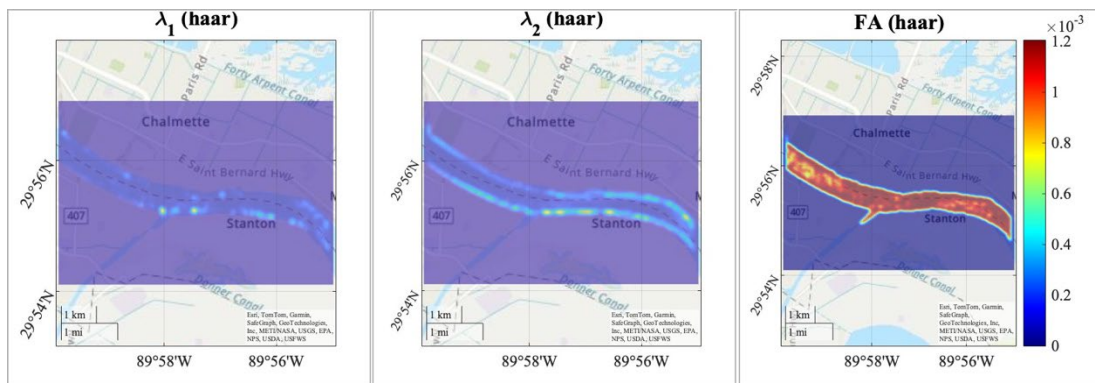


Figure 7. Eigenvalues and FA values calculated using Haar wavelet kernel

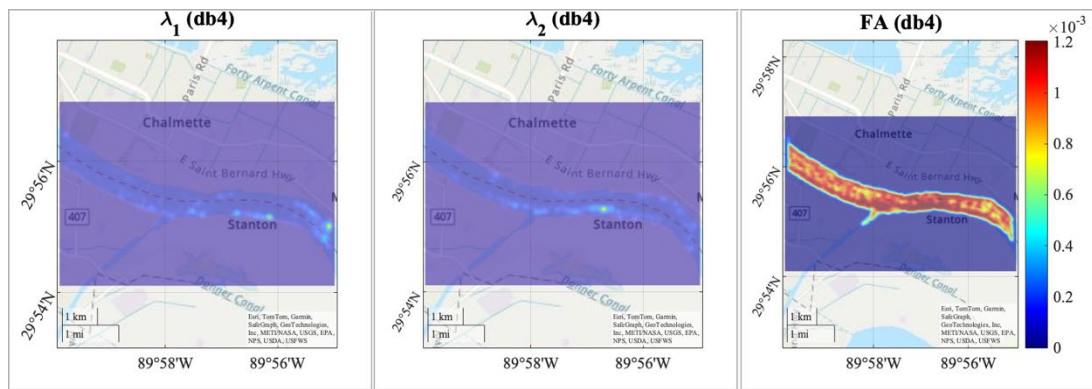


Figure 8. Eigenvalues and FA values calculated using the Db4 wavelet kernel

Figure 9 presents the fractional anisotropy (FA) distribution over the West Florida region, computed using three different wavelet kernels: *coif1*, Haar, and *db4*. The FA map derived using the *coif1* kernel exhibits a more homogeneous structure, suppressing finer details and yielding a distribution with relatively low variance. In contrast, the map generated with the Haar kernel highlights more pronounced morphological changes, particularly in the western part, and tends to generalize FA values at higher levels. The highest level of detail and local variation is observed in the map computed using the *db4* kernel, which is attributed to *db4*'s higher sensitivity to high-frequency components. These results indicate that the level of structural detail captured in FA maps is directly dependent on the choice of wavelet kernel, with *db4* being more effective in revealing micromorphological variations within the study area.

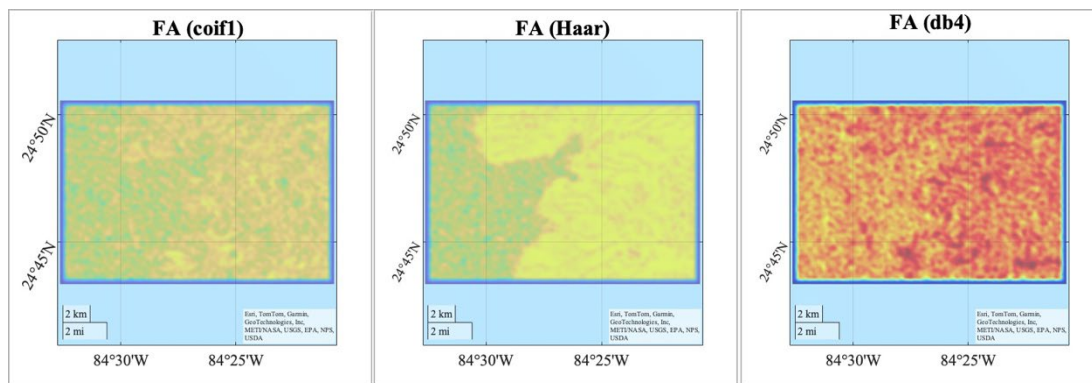


Figure 9. FA values calculated using different wavelet kernel of West Florida

In the shallow and nearly flat seabed morphology of the Sacramento-San Joaquin River Delta, it is observed that the Haar wavelet produces a homogeneous FA pattern, failing to highlight any distinctive features (Figure 10), as supported by the data shown in Table 1, where this region exhibited the highest median and kurtosis values for the Haar wavelet. With the *db4* wavelet, navigational obstacles are more easily distinguishable from the surrounding area, suggesting that *db4* could be effective for generating early warnings.

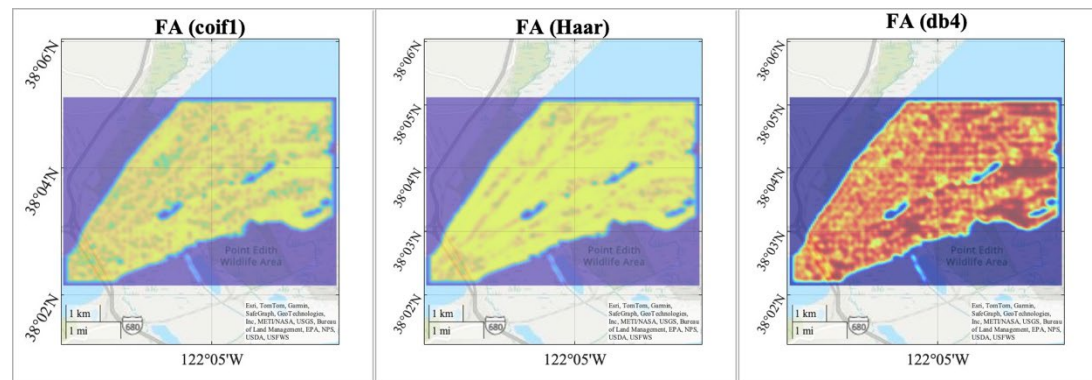


Figure 10. FA values calculated using different wavelet kernels of the Sacramento-San Joaquin River Delta

Similar patterns have also been observed in the deeper NYC region, which contains navigational obstacles; however, it is deeper than the Sacramento-San Joaquin River Delta and has a higher density of transportation activity (Figure 11).

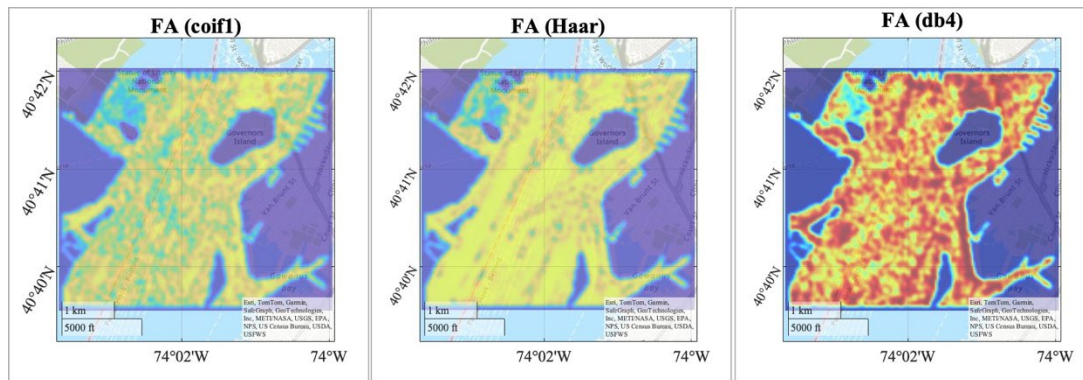


Figure 11. FA values calculated using different wavelet kernel of Upper NYC Bay

The result of the Friedman tests for all ROIs reveals a significant difference between the three FA maps, as indicated by the extremely small p-value of 4.7044e-164, allowing the rejection of the null hypothesis that all groups are equal. The mean ranks for the three maps were [1.6929 2.4583 1.8488], [1.7346 2.5164 1.7490], [1.8335 2.5674 1.5991] and [1.7362 2.4781 1.7856] respectively for ROIs:R1 to R4, with the Haar map having the highest rank, indicating it is obviously different compared to the others. To eliminate any doubt about the similarity between Coif1 and db4, the Wilcoxon signed-rank test was applied as a post-hoc test exclusively between the two maps. Although the two maps produced similar values, they are statistically significantly different from each other with $p < 0.001$ for all four regions.

3.3. Correlation Between Vessel Behavior and Seabed Isotropy

Spearman correlations for the three different FA values (obtained using coif1, Haar, and db4 wavelet kernels) were separately evaluated with respect to both SOG and C-HD using paired non-parametric tests, restricted to the MaskOverlap area. Table 5 presents Spearman's rho correlation coefficients to illustrate the relationships between kernels and SOG, and kernels and C-HD, shown column-wise. In the meandering river (ROI#1), factors affecting speed (SOG) show a slight correlation with the Haar and coif1 wavelet transforms, while db4 is less effective (rho: 0.012). In the coastal region with steep slopes and a submarine escarpment (ROI#4), there is a significant correlation with db4 (rho: 0.41) but a less significant correlation with Haar (rho: -0.02). The Haar kernel shows strong positive correlations with SOG (speed) especially in the port and delta regions (ROI#2, ROI#3).

Table 5. Spearman rank correlations (rho-values)

ROI#	Kernels	SOG	C-HD
R1	coif1	0.072	-0.10
	Haar	0.072	0.10
	db4	0.012	-0.16
R2	coif1	0.11	-0.08
	Haar	0.29	-0.20
	db4	-0.06	0.03
R3	coif1	0.12	-0.21
	Haar	0.32	-0.06
	db4	0.088	-0.12
R4	coif1	-0.51	0.10
	Haar	-0.25	-0.02
	db4	-0.38	0.41

To evaluate the discriminative power of FA (Fractional Anisotropy) as a potential feature for characterizing heading deviation, a threshold-based statistical analysis was conducted. Specifically, the dataset was partitioned into two groups for each FA threshold value ranging from zero (0) to one (1), and the corresponding heading deviation values were compared using statistical significance tests. The resulting p-values indicate whether the division based on a given FA threshold yields a meaningful separation in terms of heading deviation. The analysis was repeated for all three kernels and across all four regions. Region-specific grouped plots are presented in Figure 8.

Figure 12 illustrates the relationship between different threshold values of FA ranging between zero and one on the x-axis and their corresponding p-values on the y-axis for all three FA Maps across all four regions-of-interest. For each threshold value, the dataset is divided into two regions, and the deviation values corresponding to these regions are compared to

determine whether there is a statistically significant difference between them. The p-values on the y-axis indicate the significance level of this comparison, with lower p-values suggesting a more pronounced difference between the two regions. The p-values are near zero across all thresholds, indicating a significant difference and strong discriminatory power of FA (db4) in the bay (ROI2) and offshore (ROI4) regions. The p-values around 0.02 in the 0.2–0.4 threshold range indicate significance, but the effect weakens at other thresholds. Among all wavelets, *coif1* yields the most consistent FA performance across all ROIs and thresholds. Delta (ROI3) and Offshore (ROI4) are sensitive to the choice of wavelet and threshold, especially when using Haar wavelet.

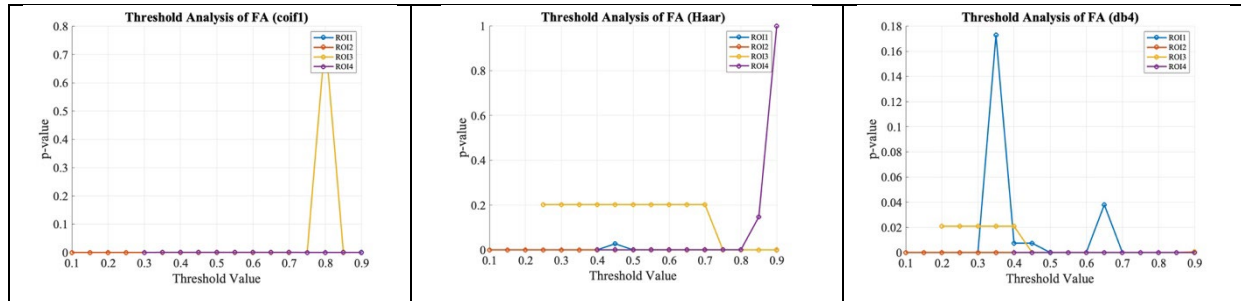


Figure 12. Threshold Analysis of FA values for COG-Heading Deviations obtained using three different wavelet kernels

Conclusions

This study demonstrated that the Haar wavelet kernel outperformed the Coiflet and db4 kernels in revealing isotropy in shallow areas near the shore, while the other kernels were more effective in modelling the middle and deeper parts of the river. The Haar wavelet, with its simplicity and computational efficiency, is suitable for basic analysis of rapidly changing data; thus, it is not surprising that the Haar wave is sensitive to riverbanks where depth changes are sharper and more abrupt. The Friedman test revealed statistically significant differences among the three FA maps, with the FA values derived from the Haar kernel being significantly higher. The DB4 kernel exhibited the highest correlation with heading deviation, particularly in offshore areas. Threshold-based analysis revealed that only the Haar kernel yielded FA values above 0.25, which were found to be distinctive for heading deviation. These findings suggest that the Haar kernel is a valuable tool for identifying isotropic features in shallow areas, while the db4 kernel is more effective in detecting anisotropic patterns related to heading deviation, especially in bay and offshore areas. *Coif1* yields more consistent FA values across different regions, making it a suitable choice for region-independent analysis.

References

- [1] K. Bergman, O. Ljungqvist, J. Linder and D. Axehill, “A COLREGs-Compliant Motion Planner for Autonomous Maneuvering of Marine Vessels in Complex Environments,” arXiv preprint, vol. 12145, 2020.
- [2] W. Mervade, “Effect of spatial trends on interpolation of river bathymetry,” *Journal of Hydrology*, vol. 371, no. 1-4, pp. 169-181, 2009.
- [3] C. Jörges, C. Berkenbrink, H. Gottschalk and B. Stumpe, “Spatial ocean wave height prediction with CNN mixed-data deep neural networks using random field simulated bathymetry,” *Ocean Engineering*, vol. 271, no. 113699, 2023.
- [4] C. Wang, M. Diao, S. Tong, L. Jiang, X. Tang and P. Jiang, “Numerical simulation study on ship manoeuvrability in mountainous rivers: Comprehensively considering effects of nonuniform flow, shallow water, narrow banks, winds and waves,” *Ocean Engineering*, vol. 306, no. 118109, 2024.
- [5] H. Hess, “Seismic anisotropy of the uppermost mantle under oceans,” *Nature*, vol. 203, p. 629–631, 1964.
- [6] M. Sormani, C. Redenbach, A. Särkkä and T. Rajala, “Second order analysis of geometric anisotropic point processes revisited,” *Spatial Statistics*, vol. 38, no. 100456, 2020.
- [7] Z. Aslan, Z. N. Caglar and D. N. Yeniçeri, “Wavelet analyses of some atmospheric parameters at black sea region,” *International Journal of Electronics Mechanical and Mechatronics Engineering*, vol. 3, no. 1, pp. 419-426, 2013.
- [8] M. Alam, G. Spadon, M. Etemad, L. Torgo and E. Milios, “Enhancing short-term vessel trajectory prediction with clustering for heterogeneous and multi-modal movement patterns,” *Ocean Engineering*, vol. 308, no. 118303, 2024.

- [9] I. Slaughter, J. L. Charla, M. Siderius and J. Lipor, "Vessel trajectory prediction with recurrent neural networks: An evaluation of datasets, features, and architectures," *Journal of Ocean Engineering and Science*, vol. 10, no. 2, p. 229–238, 2025.
- [10] H. Li, H. Jiao and Z. Yang, "Ais data-driven ship trajectory prediction modelling and analysis based on machine learning and deep learning methods," *Transportation Research Part E: Logistics and Transportation Review*, vol. 175, no. 103152, 2023.
- [11] J. Bi, M. Gao, K. Bao, W. Zhang, X. Zhang and H. Cheng, "A CNNGRU-MHA method for ship trajectory prediction based on marine fusion data," *Ocean Engineering*, vol. 310, no. 118701, 2024.
- [12] P. Kumar and E. Foufoula-Georgiou, "Wavelet analysis of geophysical applications," *Reviews of geophysics*, vol. 35, no. 4, pp. 385-412, 1997.
- [13] M. J. Wilson, B. O'Connell, C. Brown, J. C. Guinan and A. J. Grehan, "Multiscale Terrain Analysis of Multibeam Bathymetry Data for Habitat Mapping on the Continental Slope," *Marine Geodesy*, vol. 30, no. 1, p. 3–35, 2007.
- [14] A. Tommasi, B. Gibert and U. Seipold, "Anisotropy of thermal diffusivity in the upper mantle," *Nature*, vol. 411, p. 783–786, 2001.
- [15] İ. Öz, "Comparative Analysis of Wavelet Families in Image Compression, Featuring the Proposed New Wavelet," *TJST*, vol. 19, no. 1, p. 279–294, 2024.
- [16] F. Csillag and S. Kabos, "Wavelets, boundaries, and the spatial analysis of landscape pattern," *Écoscience*, vol. 9, no. 2, pp. 177-190, 2002.
- [17] R. M. Neupauer, K. L. Powell, X. Qi, D. H. Lee and D. A. Villhauer, "Characterization of permeability anisotropy using wavelet analysis," *Water Resources Research*, vol. 42, no. W07419, 2006.
- [18] Y. Guo, R. Zhao, Y. Zeng, Z. Shi and Q. Zhou, "Identifying scale-specific controls of soil organic matter distribution in mountain areas using anisotropy analysis and discrete wavelet transform," *Catena*, vol. 160, pp. 1-9, 2018.
- [19] F. Bedoya-Maya, P. Shobayo, A. Nicolet, E. Christopoulou, I. Majoor, E. Hassel and T. Vanelslander, "Cargo consolidation in port-hinterland container transport: A spatial economic assessment for inland waterways," *Research in Transportation Business & Management*, vol. 59, no. 101254, 2025.
- [20] M. O'Neil, D. Taillie, B. Walsh, W. C. Dennison, E. K. Bone, D. J. Reid, R. Newton, D. L. Strayer, L. Boicourt, L. B. Birney, S. Janis, P. Malinowski and M. Fisher, "New York Harbor: Resilience in the face of four centuries of development," *Regional Studies in Marine Science*, vol. 8, no. 2, pp. 274-286, 2016.
- [21] "About the Watershed," U.S. Environmental Protection Agency, [Online]. Available: <https://www.epa.gov/sfbay-delta/about-watershed>. [Accessed 31 05 2025].
- [22] H. Robert, "Bathymetry of the Straits of Florida and Bahama Islands Part III. Southern Straits of Florida," *Deep Sea Research and Oceanographic Abstracts*, vol. 12, no. 6, p. 1052, 1965.
- [23] NOAA NCEI, "Bathymetric Data Viewer," [Online]. Available: <https://www.ncei.noaa.gov/maps/bathymetry/>. [Accessed 05 01 2025].
- [24] N. Ritter and M. Ruth, "The GeoTIFF data interchange standard for raster geospatial image data. U.S. Geological Survey," [Online]. Available: <https://www.remotesensing.org/geotiff/geotiff.html>. [Accessed 1997].
- [25] U.S. Department of Commerce, "Marine Cadastre AIS Data," National Oceanic and Atmospheric Administration (NOAA), [Online]. Available: <https://marinecadastre.gov>. [Accessed 22 03 2025].
- [26] E. Ross, C. Astrup, E. Bitner-Gregersen, N. Bunn, G. Feld, B. Gouldby, A. Huseby, Y. Liu, D. Randell, E. Vanem and P. Jonathan, "On environmental contours for marine and coastal design," *Ocean Engineering*, vol. 195, no. 106194, 2020.
- [27] T. Emmens, C. Amrit, A. Abdi and M. Ghosh, "The promises and perils of Automatic Identification System data," *Expert Systems with Applications*, vol. 178, no. 114975, 2021.

- [28] E. Tu, G. Zhang, L. Rachmawati, E. Rajabally and G. B. Huang, "Exploiting AIS Data for Intelligent Maritime Navigation: A Comprehensive Survey from Data to Methodology," *IEEE Transactions on Intelligent Transportation Systems*, vol. 19, no. 5, pp. 1559-1582, 2018.
- [29] M. Chaudhary and A. Dhamija, "A brief study of various wavelet families and compression techniques," *Journal of Global Research in Computer Sciences*, vol. 4, no. 4, p. 43-49, 2013.
- [30] L. Debnath and F. A. Shah, *Wavelet transforms and their applications*, Birkhauser, 2015.
- [31] D. L. Donoho, "De-noising by soft-thresholding," *IEEE Transactions on Information Theory*, vol. 41, no. 3, pp. 613 - 627, 2002.
- [32] M. Unser, "Texture classification and segmentation using wavelet frames," *IEEE Transactions on Image Processing*, vol. 4, no. 11, p. 1549-1560, 1995.
- [33] A. Akl and J. Iskandar, "Second-moment matrix adaptation for local orientation estimation," in *International Conference on Systems, Signals and Image Processing (IWSSIP)*, Bratislava, 2016.
- [34] Z. Liu, W. Qi, S. Zhou, W. Zhang, C. Jiang, Y. Jie, C. Li, Y. Guo and J. Guo, "Hybrid deep learning models for ship trajectory prediction in complex scenarios based on ais data," *Applied Ocean Research*, vol. 153, no. 104231, 2024.

Article Information Form

Authors Contributions

Füsün Er: Collected data, developed software, conducted the experimental analysis, interpreted the data and results, and drafted the manuscript.

Şengül Ersoy: Developed the mathematical background for the study, interpreted the results, and drafted the manuscript.

Yıldırım Yalman: Conceptualized the study, made critical revision of the manuscript, interpreted the data, supervised the research.

Conflict of Interest Notice

The authors declare that there is no conflict of interest regarding the publication of this paper.

Support/Supporting Organizations

This study is part of the project entitled as "Investigation and Optimization of AIS and Bathymetry Data Using Data Fusion Methods for Computer-Aided Ship Route Planning" (STB Project Code:100611), supported by Piri Reis University.

Ethical Approval

It is declared that during the preparation process of this study, scientific and ethical principles were followed, and all the studies benefited from are stated in the bibliography.

Availability of data and material

Not applicable

Artificial Intelligence Statement

No artificial intelligence tools were used while writing this article.

Plagiarism Statement

This article has been scanned by iThenticate™.